Grain boundary wetting during magma migration by two-phase flow

Saswata Hier-Majumder, Yanick Ricard, David Bercovici

Grain boundary wetting during magma migration by two-phase flow

Saswata Hier-Majumder *, Yanick Ricard [1], David Bercovici

Department of Geology and Geophysics, Yale University, New Haven, CT, USA

Abstract

We employ the theory of two-phase flow to investigate the influence of grain boundary wetting during segregation of magma in a partially molten aggregate. In partially molten aggregates the 'disaggregation melt fraction', the volume fraction of partial melt at which grain boundaries are completely wetted, is crucial in determining the total interfacial force per unit volume. Surface tension on grain boundaries in melt fractions less than the disaggregation melt fraction tend to homogenize melt distribution when the solid-liquid interfacial tension is smaller than the interfacial tension arising from grain boundaries. We also demonstrate that in the presence of large grain-grain interfacial tension, the solitary wave solution to the mass, energy, and momentum equations for two-phase aggregates becomes dissipative. Under such conditions, the rate of buoyancy driven melt segregation is reduced due to melt retention by grain boundaries.

Key words: Two-phase flow, partial melting, nonlinear waves, magma transport, grain boundary wetting.

1 Introduction

Formation and migration of melts is a crucial process in the geodynamical and geochemical evolution of planetary interiors. Partial melting reduces the viscosity of the silicate-melt aggregates (1; 2) and also extracts incompatible elements from mantle source regions. While migrating from these source

* Corresponding Author
Email address: saswata.hier-majumder@yale.edu (Saswata Hier-Majumder).
[1] Also at: Laboratoire de Science de la Terre, Ecole Normale Supérieure de Lyon, Lyon, France

regions, partial melts may react with the surrounding mantle, eventually revealed as the chemical signature of the mantle in the lava erupted on the surface. The rate and volume of melt ascent through the mantle is also reflected in the periodicity of magma emplacement and the volumes of magma provinces.

A dynamic balance between several forces occurring on both small and large length scales dictates the mechanism of magma transport through the planetary interiors. For example, interfacial tension on grain boundaries and grain-melt interfaces in partially molten rocks influence melt migration and melt distribution in planetary interiors. In particular, transport of partial melt by porous flow takes place through a network of micron-sized interconnected tubules and sheets. The backscattered electron micrograph in Figure 1 illustrates such a network of tubules in an experimentally annealed olivine-water aggregate (3, run M132). The flux of melt through this network is controlled by the geometry of the network, namely the shape and connectivity of the tubules and sheets. The geometry of the network is influenced in turn by the surface tension on grain boundaries and the melt-grain interfaces (4). Grain boundary capillary forces can also influence melt extraction from a magma source region. Although gravity drives low-density, low-viscosity melts away from the source region, melt extraction is likely to be retarded by the retention of melts as thin films along grain boundaries and thin filaments along grain edges (5). Thus the balance between grain-grain interfacial tension and gravity controls the mode of melt migration. Finally, the retained melt experiences a longer residence time near its source region, compared to the extracted melt. Consequently, the chemical signature of these two melts derived from chemical exchange with the surrounding rocks, can be significantly different, despite the common origin of both melt fractions.

In this work we present a theoretical analysis of the influence of grain-grain interfacial tension on melt segregation in a solid-liquid aggregate. We employ the continuum theory of two-phase flow (6; 7; 8), modified to accommodate interfacial physics including surface tension (9; 10; 11). In this formulation we recognize that the total surface tension of a solid-liquid aggregate depends on the volume fraction of liquid present. For melt fractions lower than a critical amount, the melt resides primarily in tubules along three grain junctions and four grain corners, but at melt fractions above this critical limit, the solid grains are completely surrounded by melt and grain boundaries cease to exist. We call this critical fraction as the 'disaggregation melt fraction'. At melt fractions less than the disaggregation melt fraction, both solid-solid and solid-liquid interfaces contribute to the total surface tension, whereas at melt fractions above the disaggregation melt fraction, only solid-fluid interfaces contribute to the total interfacial tension.

The influence of interfacial tension on segregation and redistribution of melts

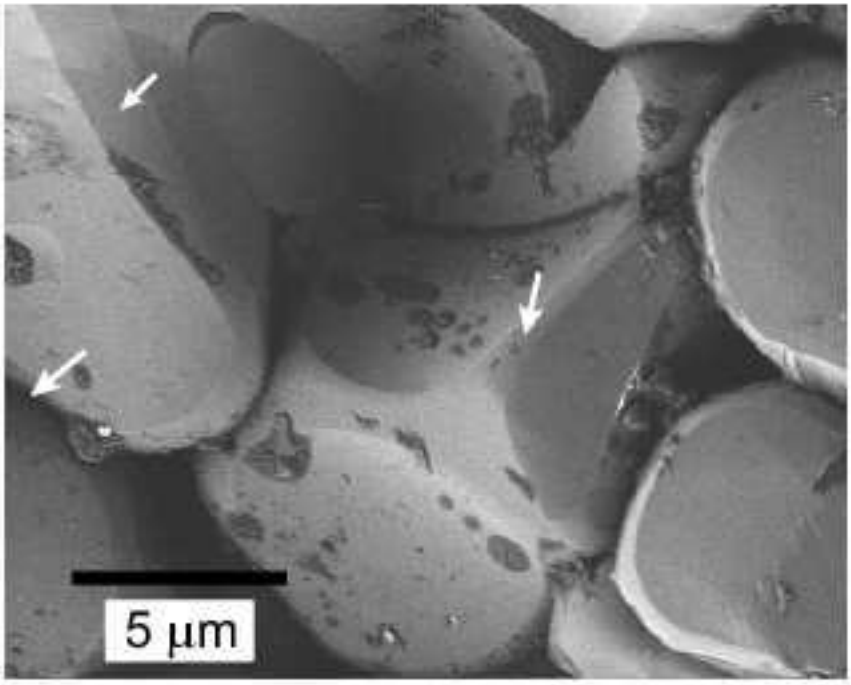

Fig. 1. A backscattered electron image of an aggregate of olivine and water annealed under hydrostatic condition at a pressure of 5 GPa and a temperature of 1373 K. Notice the network of tubules along the edges of the grains.

in solids under a hydrostatic condition of stress has been investigated both experimentally (12; 13) and theoretically (14; 9; 10; 11; 15). Experimental work (12; 13) has addressed the influence of the grain-grain interfacial tension on melt distribution. However, due to the small length scales of the experimental samples, buoyancy effects were negligible compared to interfacial tension effects. Theoretical work (14; 9; 10; 11; 15), however, has addressed the importance of the interfacial tension without recognizing the presence of a disaggregation melt fraction. In these analyses the total interfacial tension is treated as a continuous function of the melt fraction, whose effect vanishes in the absence of melts. While such a description is realistic for a mixture of two immiscible liquids, it fails to account for the presence of interfacial tension on grain boundaries. In planetary interiors, the rise of magma through columns of rock is likely to be influenced by interfacial forces arising from grain boundaries as well as buoyancy. Thus a complete description of the melt migration processes should incorporate both grain-grain interfacial tension and gravity.

In this work we develop and investigate a two-phase theory which includes the influence of grain boundaries on melt redistribution. We compare the modes of buoyant rise of magma in the presence and absence of strong grain boundary forces. We discuss the possibility of melt retention by grain boundaries and the possible implications in mantle metasomatism.

2 Formulation

Consider a solid-melt aggregate containing a small fraction of melt, residing primarily in a network of interconnected tubules along triple grain junctions and grain edges. In this work we will use the mass, momentum and energy conservation equations for a two-phase aggregate discussed in (author?) (16). We assume no mass exchange (melting or solidification) takes place between the solid matrix and the melt. Throughout the rest of the paper, we will use the subscripts f and m to indicate the fluid (partial melt) and the viscous solid matrix, respectively.

Interfacial force in a two-phase aggregate is proportional to the average interfacial area per unit of the control volume. Since the interfacial area is averaged over a control volume containing several grains and melt pockets and yet not large enough to exhibit any significant variation of the field variables, the location and geometry of the interfaces within the control volume remain unknown. When only one interface between the two phases is present (such as in two immiscible liquids), the interfacial force can be expressed as σa, where σ is a temperature dependent surface tension and a is the interfacial area density, dependent only on ϕ (9). One important property of a is $a \to 0$ as $\phi \to 0, 1$, corresponding to each individual phase constituting the entire aggregate. However, when one of the fluid phases is actually a viscous solid with grain boundaries, the presence of grain boundaries in the unmelted matrix require $a \neq 0$ when $\phi = 0$. In order to address this issue, and yet bearing in mind that a description of the interfacial area requiring detailed knowledge of the position of the interfaces in untenable in the present scope of the theory, we take the following approach:

total interfacial force per unit volume is expressed as a sum of the interfacial forces on the solid-solid interfaces (grain boundaries) and solid-liquid (grain-melt) interfaces. This quantity is described as $\chi = \sigma_{ss} a_{ss} + \sigma_{sl} a_{sl}$, where subscript '*ss*' indicates solid-solid and '*sl*' indicates solid-liquid interfaces. Next, in order to define a functional form of χ, we use a simple geometric model within a control volume described in Appendix A. We also demonstrate such an approach does not violate the fundamental energy conservation rules in appendix B. Essentially, this approach treats the grain-grain interfaces as a limiting case of two grain-melt interfaces, placed an infinitesimaly small distance away, separated by an infinitesimally thin melt film.

Consider a partially molten aggregate containing a spatially and temporally variable melt fraction ϕ. In this aggregate, both the solid matrix and and the melt flow as viscous fluids with viscosities μ_m and μ_f, while their respective velocities are given by the quantities $\mathbf{v_m}$ and $\mathbf{v_f}$. The densities of the matrix and the fluid phases are given by ρ_m and ρ_f, respectively. We treat the pressures of the matrix and the fluid as independent quantities given by P_m and P_f.

The mass conservation equations for both phases are given by:

$$\frac{\partial \phi}{\partial t} + \nabla \cdot (\phi \mathbf{v_f}) = 0, \tag{1}$$

$$\frac{\partial (1-\phi)}{\partial t} + \nabla \cdot ((1-\phi)\mathbf{v_m}) = 0. \tag{2}$$

We also assume that the fluid viscosity is negligible compared to the matrix viscosity ($\mu_f = 0$), in which case the interfacial forces are supported entirely by the matrix (16). Under this condition, the momentum equation for each individual phase is given by (9; 16):

$$0 = -\phi(\nabla P_f + \rho_f g\hat{y}) + c\Delta \mathbf{v}, \tag{3}$$

$$0 = -(1-\phi)(\nabla P_m + \rho_m g\hat{y}) - c\Delta \mathbf{v} + \nabla \cdot \left((1-\phi)\underline{\tau_m}\right) + (\Delta P \nabla\phi + \nabla\chi). \tag{4}$$

The interaction coefficient c arises from viscous interaction at the fluid-matrix interface and is inversely proportional to the permeability (9, see also Section 2.3).

The constitutive relation for the matrix is given by,

$$\underline{\tau_m} = \mu_m \left(\nabla \mathbf{v_m} + [\nabla \mathbf{v_m}]^\dagger - \frac{2}{3}\nabla \cdot \mathbf{v_m}\underline{\mathbf{I}}\right) \tag{5}$$

The stress drop condition is given by:

$$\frac{\partial \chi}{\partial \phi} = -\Delta P - \frac{K_0 \mu_m}{\phi(1-\phi)} \frac{D_m \phi}{Dt}, \tag{6}$$

where K_0 is a dimensionless constant of $O(1)$ and the material derivative D_m/Dt is given by:

$$\frac{D_m}{Dt} = \frac{\partial}{\partial t} + \mathbf{v_m} \cdot \nabla. \tag{7}$$

The quantity on the left hand side of equation (6) represents reversible surface energy (*i.e* interfacial tension) and the quantities on the right hand side represent work exerted by the pressures with the irreversible work from isotropic viscous compaction removed. We derive equation (6), from the neergy conservation equation in appendix B.

Equations (1)-(6) provide the complete set of governing equations for the following seven variables, $\mathbf{v}_f$, $\mathbf{v}_m$, $\underline{\tau}_m$, χ, ϕ, P_f, and P_m. However, in order to close the equations, an additional relation between χ and one of the unknowns is necessary. Notice that the quantity $\nabla\chi$ in equation (4) and the quantity $\partial\chi/\partial\phi$ in equation (6) appears as $\nabla\sigma a$ and $\sigma(\partial a)/(\partial\phi)$, in the formulation given in reference (9), in which only interfacial tension arising from the solid-liquid interface is considered.

The volume fraction of the fluid controls the proportion of solid-solid and solid-liquid interfaces. Below a critical melt fraction the melt resides in tubules along grain edges and wets a fraction of the grain boundary. We refer to this critical melt fraction as the 'disaggregation melt fraction', since the matrix desegregates at melt fractions greater than or equal to this melt fraction. At fluid volume fractions less than the disaggregation melt fraction, both the solid-solid and solid-melt interfacial tensions contribute to χ. At the disaggregation melt fraction, the grain boundaries are completely wetted, and the only interface present is the solid-liquid interface. As the simple derivation in appendix A indicates, the relationships between χ and ϕ below and above the disaggregation melt fraction are given by:

$$\chi(\phi) = \begin{cases} a_0 \left[\sigma_{sl}\chi_1\sqrt{\phi} + \sigma_{ss}\left(1 - \chi_2\sqrt{\phi}\right)\right] & \text{if } \phi < \phi_s, \\ \\ \sigma_{sl} a_0 \sqrt{\frac{\pi}{4}(1-\phi)} & \text{if } \phi \geq \phi_s, \end{cases} \tag{8}$$

where χ_1 and χ_2 are parameters dependent on the solid-solid and the solid-melt interfacial energies. The quantity a_0 is the reciprocal of the average grain size, as indicated in the micromechanical model in Appendix A, and ϕ_s is the disaggregation melt fraction. Although in this work we employ a relatively simple model of melts along the grain boundaries, very similar results are obtained from analyses with a tetrakaidecahedral geometry of the solid grains (4).

The forces governing the conservation of momentum of two phase aggregates are proportional to the gradients of matrix and fluid pressures as evidenced in equation (4) and (3). While the first derivative of χ with respect to ϕ, χ', is proportional to the pressures, the second derivative χ'', is proportional to the pressure gradients and indicates the gradient of total interfacial tension. When χ'' is positive, the interfacial force tends to drive melt in to low pressure regions

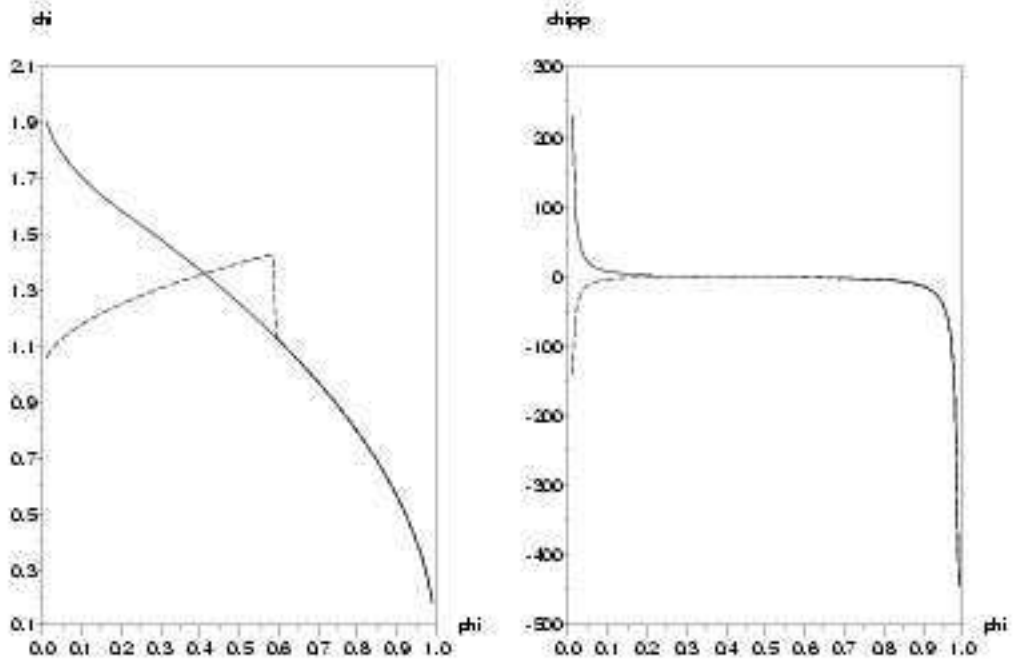

Fig. 2. Plots of total surface tension χ and χ'' as a function of ϕ. The solid and broken curves correspond to $\kappa = 2$ and 1, respectively.

by capillary action. This can be achieved when the grain-grain interfacial force is stronger compared to the grain-melt interfacial force. Figure 2 depicts χ and the second derivative of χ as a function of ϕ for two such cases. In the curve for $\kappa = 2$, interfacial tension on grain boundaries is the maximum as allowed by the scenario described in Appendix A, and χ'' is positive for melt fractions below the disaggregation melt fraction. For $\kappa = 1$, as well as for melt fractions greater than the disaggregation melt fraction, $\chi'' < 0$, indicating that the surface tension attracts melts into the region of high melt pessure.

2.2 One-dimensional equations

In this work we solve the system of equations (1)-(6), along with the interfacial tension relation (8) in one-dimension in a domain of dimension $2l$. To arrive at the one-dimensional equations, we take the general governing equations (1)-(6), and consider the case where the only nonzero motion and gradients are along the vertical (y) direction. The boundary conditions for the velocities of both phases are given by,

$$v_{my} = v_{fy} = 0 \text{ at } y = \pm l \tag{9}$$

and the initial melt distribution is,

$$\phi(y,0) = \phi_0(y). \tag{10}$$

The sum of the mass conservation equations (1) and (2), combined with boundary conditions for vertical velocities yields

$$\phi v_{fy} + (1-\phi) v_{my} = 0. \tag{11}$$

The equation for mass conservation of the matrix yields,

$$\frac{\partial \phi}{\partial t} = \frac{\partial}{\partial y}\left((1-\phi) v_{my}\right). \tag{12}$$

We can eliminate the pressures of the individual phases by combining momentum conservation equations (3) and (4), to obtain the action-reaction equation given by,

$$0 = \nabla\left(\chi - (1-\phi)\Delta P\right) + \nabla\left((1-\phi)\underline{\tau}_m\right) - (1-\phi)\Delta\rho g\hat{y} - \frac{c\,\Delta v}{\phi}. \tag{13}$$

Making the substitution $\Delta v_y = v_{my}/\phi^2$ based on equation (11), the y component of the action-reaction equation (13) leads to

$$0 = \frac{\partial}{\partial y}\left(\chi - (1-\phi)\left(\Delta P + \frac{4}{3}\mu_m \frac{\partial v_{my}}{\partial y}\right)\right) - (1-\phi)\Delta\rho g - \frac{c v_{my}}{\phi^2}. \tag{14}$$

We employ the equation for conservation of matrix mass to yield,

$$\frac{D_m \phi}{Dt} = (1-\phi)\frac{\partial v_{my}}{\partial y}, \tag{15}$$

which we use to rewrite the stress drop equation (6),

$$\Delta P = -\left(\chi' + \frac{K_0 \mu_m}{\phi}\frac{\partial v_{my}}{\partial y}\right). \tag{16}$$

We substitute ΔP into the action-reaction equation (14) to obtain,

$$0 = \frac{\partial}{\partial y}\left(\chi + (1-\phi)\chi' + \mu_m\left(\frac{K_0}{\phi} + \frac{4}{3}\right)(1-\phi)\frac{\partial v_{my}}{\partial y}\right) - (1-\phi)\Delta\rho g - \frac{c v_{my}}{\phi^2} \tag{17}$$

By solving equations (17) and (12), all the unknowns can be determined.

We nondimensionalize velocity, length, and surface tension according to the relations:

$$v_m = \frac{\rho_m g \delta_m^2}{\mu_m} w, \quad y = \delta_m y^*, \quad \chi = \sigma_{sl}\, a_0\, \chi^*. \tag{18}$$

The length scale used in the nondimensionalization is the matrix compaction length $\delta_m = \sqrt{(4\mu_m)/(3c)}$. Also, adding the constraint $K_0 = 4/3$, equations (12) and (17) can be nondimensionalized into

$$\frac{\partial \phi}{\partial t} = \frac{\partial}{\partial y}\left((1-\phi)w\right) \tag{19}$$

$$0 = \xi \frac{\partial}{\partial y}\left(\chi + (1-\phi)\chi'\right) + \frac{4}{3}\frac{\partial}{\partial y}\left(\frac{(1-\phi^2)}{\phi}\frac{\partial w}{\partial y}\right) - R(1-\phi) - \frac{4}{3}\frac{w}{\phi^2}. \tag{20}$$

The nondimensional quantities are given by,

$$\xi = \frac{\sigma_{sl}\, a_0}{\rho_m g \delta_m}, \quad R = \frac{\Delta\rho}{\rho_m}. \tag{21}$$

The compaction length δ_m, depends on the matrix viscosity μ_m and the interaction coefficient c. For negligibly small viscosity of the melt, the interaction coefficient $c = \mu_f \phi^2/k$, where k is the permeability (9, Section 4.3). Employing a simple model of melt percolation through tubules along grain edges, one obtains $k = \phi^2/72\pi a_0^2$, where $1/a_0$ is the grain size (17, Section 9.3). Thus we obtain $c \approx 10^{10}$ Pa s m^{-2}, for a melt viscosity $\mu_f = 1$ Pa s and a grain size $1/a_0 = 100\mu$m. Thus, we obtain a matrix compaction length $\delta_m = 10$ km, for a matrix viscosity $\mu_m = 10^{18}$ Pa s. We have also assumed $\Delta\rho = 300$ kg m^{-3} and $\rho_m = 3 \times 10^3$ kg m^{-3}, leading to $R = 0.1$. The selection of the parameters also implies that nondimensional unit matrix velocity and time are equivalent to dimensional matrix velocity and time of 3×10^{-6}m s^{-1} (≈ 100myr^{-1}) and 3.3×10^9 s (≈ 100 yr), respectively. In this work we examine the influence of surface tension in the numerical experiments by using different values of ξ between 10^{-6} to 10^{-3}.

3 Results

We employ equations (19) and (20) to solve for the matrix velocity w and the melt fraction ϕ. We obtain an analytical solution for the linearized form of equation (17), while the complete nonlinear equation is solved numerically

using the finite volume method with an explicit time marching scheme. The numerical solutions for self-separation in the absence of gravity were obtained for a zero velocity boundary condition (*i.e.* velocity of both phases are zero at the top and the bottom). The solutions in the presence of gravity are obtained for a periodic boundary condition.

3.1 Marginal stability analysis

We linearize equations (19) and (20), by adding small perturbations $\phi_1(y,t)$ and $w_1(y,t)$ to constant background values ϕ_0 and w_0. The dependent variable χ can be expressed by a Taylor series expansion near the background value. Thus, the variables in the perturbed state are given by,

$$\begin{aligned} \phi &= \phi_0 + \epsilon\phi_1, \quad w = w_0 + \epsilon w_1, \\ \chi &= \chi(\phi_0) + \epsilon\chi_0'\phi_1, \quad \chi' = \chi_0' + \epsilon\chi_0''\phi_1, \end{aligned} \tag{22}$$

where $\chi_0' = \chi'(\phi_0)$. In order to determine the background melt fraction and velocity, we replace the perturbed variables from equation (22) into equations (19) and (20). Dropping the subscript 1, and dropping terms containing the second or higher powers of ϵ, we obtain the linearized equations,

$$\frac{\partial w}{\partial y} = \frac{1}{1-\phi_0}\left(\frac{\partial \phi}{\partial t} + w_0\frac{\partial \phi}{\partial y}\right), \tag{23}$$

$$\begin{aligned} 0 = \epsilon\Bigg[\xi(1-\phi_0)\chi_0''\frac{\partial \phi}{\partial y} + \frac{4}{3}\left(\frac{1+\phi_0}{\phi_0}\right)\left(\frac{\partial^2\phi}{\partial t\partial y} + w_0\frac{\partial^2\phi}{\partial y^2}\right) + \\ R\phi - \frac{4}{3}\left(\frac{w}{\phi_0^2} - 2\frac{w_0\phi}{\phi_0^3}\right)\Bigg] - R(1-\phi_0) - \frac{4}{3}\frac{w_0}{\phi_0^2}, \end{aligned} \tag{24}$$

which yields on the zeroth order

$$w_0 = -\frac{3R}{4}\phi_0^2(1-\phi_0). \tag{25}$$

We take $O(\epsilon)$ equations and substitute ϕ of the form

$$\phi_1 = \bar{\phi}\exp(st)\exp i(ky - \omega t), \tag{26}$$

yielding a growth rate s,

$$s = -\frac{3}{4}\,\frac{\xi\,\chi_0''\,\phi_0^2\,(1-\phi_0)^2\,k^2}{1+\phi_0(1-\phi_0^2)k^2}. \tag{27}$$

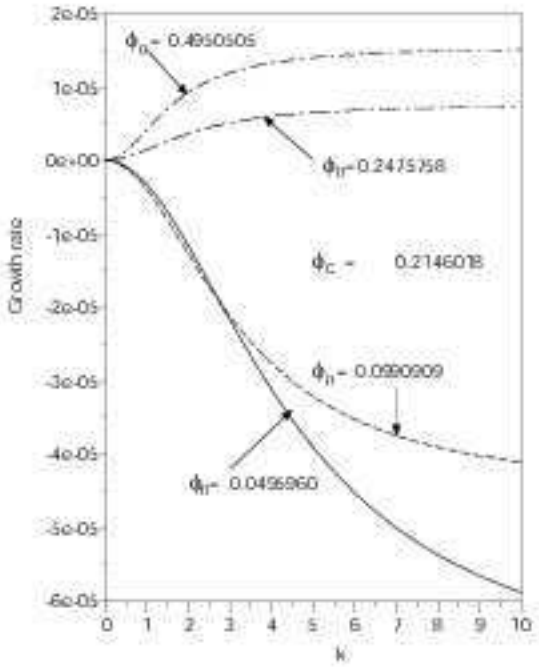

Fig. 3. Results from the linear analysis. Growth rate of melt perturbations, as a function of nondimensionalized wavenumber. Each curve corresponds to a different value of melt fraction in the unperturbed state marked in the plots.

The dispersion relation between the frequency and the wavenumber is given by,

$$\omega = -\frac{3Rk}{4}\left(\frac{\phi_0\,(1-\phi_0)\,(2-3\phi_0)}{1+\phi_0(1-\phi_0^2)k^2} - (1-\phi_0)\,\phi_0^2\right). \tag{28}$$

The dispersion relation (28) leads to the phase and group velocities $U_{ph} = \omega/k$ and $U_g = \partial\omega/\partial k$, respectively.

The plots in Figure 3 display the growth rate of the traveling waves as a function of the nondimensional wave number k, for four different values of ϕ_0, the background melt fraction, and for $\kappa = 2$, implying the presence of strong grain-grain interfacial tension. The different curves in the plot of the growth rate as a function of k, indicates that the sign of the growth rate depends on melt fraction, and it changes from negative to positive as the melt fractions increases above the disaggregation melt fraction. The change in the sign of the growth rate is caused by the change in the sign of the second derivative of the surface tension, as depicted in the curve for $\kappa = 2$ Figure 2(b). The quantity χ'' is proportional to the gradient of surface tension forces. A positive value of χ'' implies that the total interfacial force drives melt into low pressure regions, whereas a negative value indicates that the interfacial force attracts melt from low pressure into high pressure region. Strong interfacial tension force on grain boundaries renders the quantity χ'' positive at melt fractions below the disaggregation melt fraction.

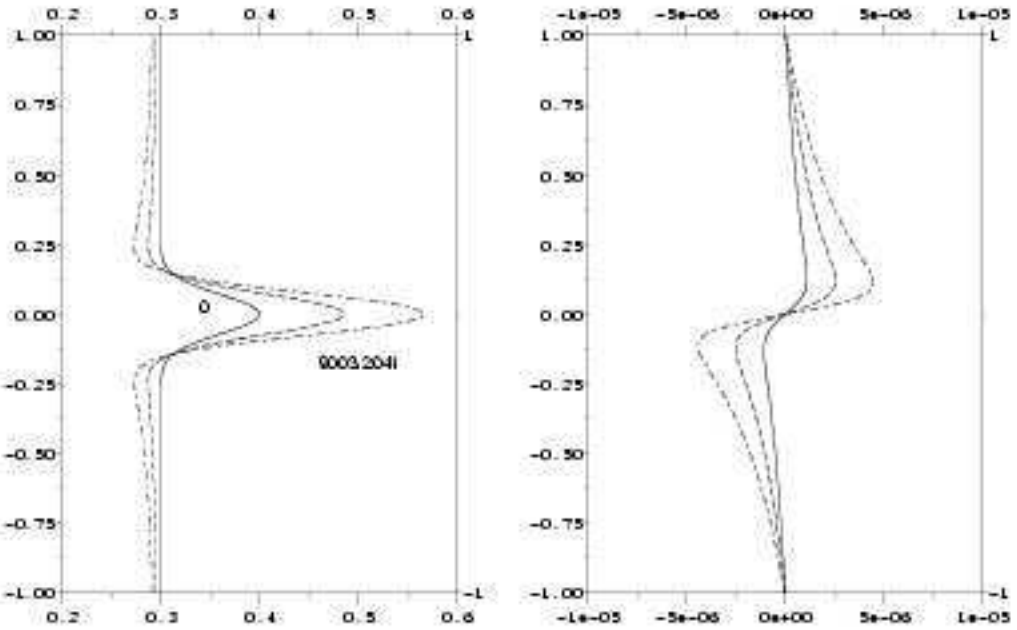

Fig. 4. Self-separation of the melt driven by solid-liquid interfacial tension. Notice that the initial background porosity is larger than the disaggregation melt fraction, indicating the presence of only the solid-melt interface.In this plot $\xi = 10^{-3}$.

3.2 Nonlinear analysis

In this section we present solutions to the nonlinear equations (19) and (20). We discuss the influence of grain boundary wetting in the evolution of melt perturbations in the absence of gravity in section 3.2.1 and demonstrate the simultaneous influence of grain boundary wetting and gravity on ascending melt perturbations in section 3.2.2.

3.2.1 Self separation

In the absence of gravitational force and deformation, the surface tension forces are balanced by the pressure difference between the solid and the fluid phases. Figures 4- 6 demonstrate the evolution of an initial perturbation in melt distribution with time. In all three of these plots, the length of the domain is equal to twice the compaction length of the matrix. The values of parameters R and ξ are 0 and 1×10^{-3} for all three plots. To demonstrate the influence of grain boundaries, we chose $\kappa = 2$, the maximum permissible value according to the model presented in Appendix A.

The plot of melt distribution at several time steps depicted in Figure 4(a)

illustrates surface tension driven self separation of the melt. In this case the initial melt distribution is given by a Gaussian perturbation with a background value larger than the disaggregation melt fraction. Under such a condition, no grain boundaries are present and the result is similar to that obtained by previous works (10; 11; 16). The dimensional length of the region in the plot is 20 km. Dimensionalization of the length and timescales in the plots indicate that an approximately 3 km wide sill containing around 55 volume% melt can be generated over a time period of 900 ka, while the matrix flows with maximum velocities in the order of 500 microns yr^{-1} near the sill. The time evolution of the matrix velocity depicted in Figure 4(b) demonstrates that the matrix velocity is always fastest at the flank of the perturbation, corresponding to the steepest gradient in the melt distribution. Consequently, melt gets drained through these regions most quickly, as seen in Figure 4(a). Notice also, with increasing time, the width of the melt-rich region increases.

The pattern of melt segregation is remarkably different when the background melt fraction is below the disaggregation melt fraction and the peak melt fraction above the disaggregation melt fraction (Figures 5 a and b). In Figure 5(a) the background region remains almost undepleted while the initial perturbation grows at its own expense. The initially 6 km thick perturbation narrows down to a maximum thickness of 4 km in 700 ka. As revealed in the plot of velocity distribution in Figure 5(b), the matrix velocity is still highest at the flanks of the initial perturbation. However, with time the melt from the flank is drained into the peak of the perturbation causing the perturbation to shrink in width. The most important feature in this case is the extremely slow melt extraction from the background. The enlarged view plot of the melt distribution in Figure 5(c) illustrates that melt from the flank of the perturbation is drained into the peak as well as into the background. However, as the total melt fraction in the peak increases, melt is slowly drawn back into the peak. Therefore, the background melt fraction remains largely unaltered. Since the background melt fraction is below the critical limit, a fraction of the grain boundaries in these regions are unwetted. The unwetted grain boundaries exert surface tension on the melt, which acts against the driving force for segregation arising from the solid-liquid interfacial force. As a consequence, complete draining of the melt will be practically impossible. This observation also contrasts the observation from previous formulations where it was possible to drain the entire amount of fluid from the matrix in the absence of grain boundaries (10; 11; 16).

Perturbations in melt distribution are rapidly homogenized by grain boundary wetting, when both the peak and background melt fractions are less than the disaggregation melt fraction. The plots of melt distribution and matrix velocity distribution in Figure 6 demonstrate the homogenization caused by grain boundary wetting. In this plot both the background and the peak perturbations are below the disaggregation melt fraction, which is homogenized

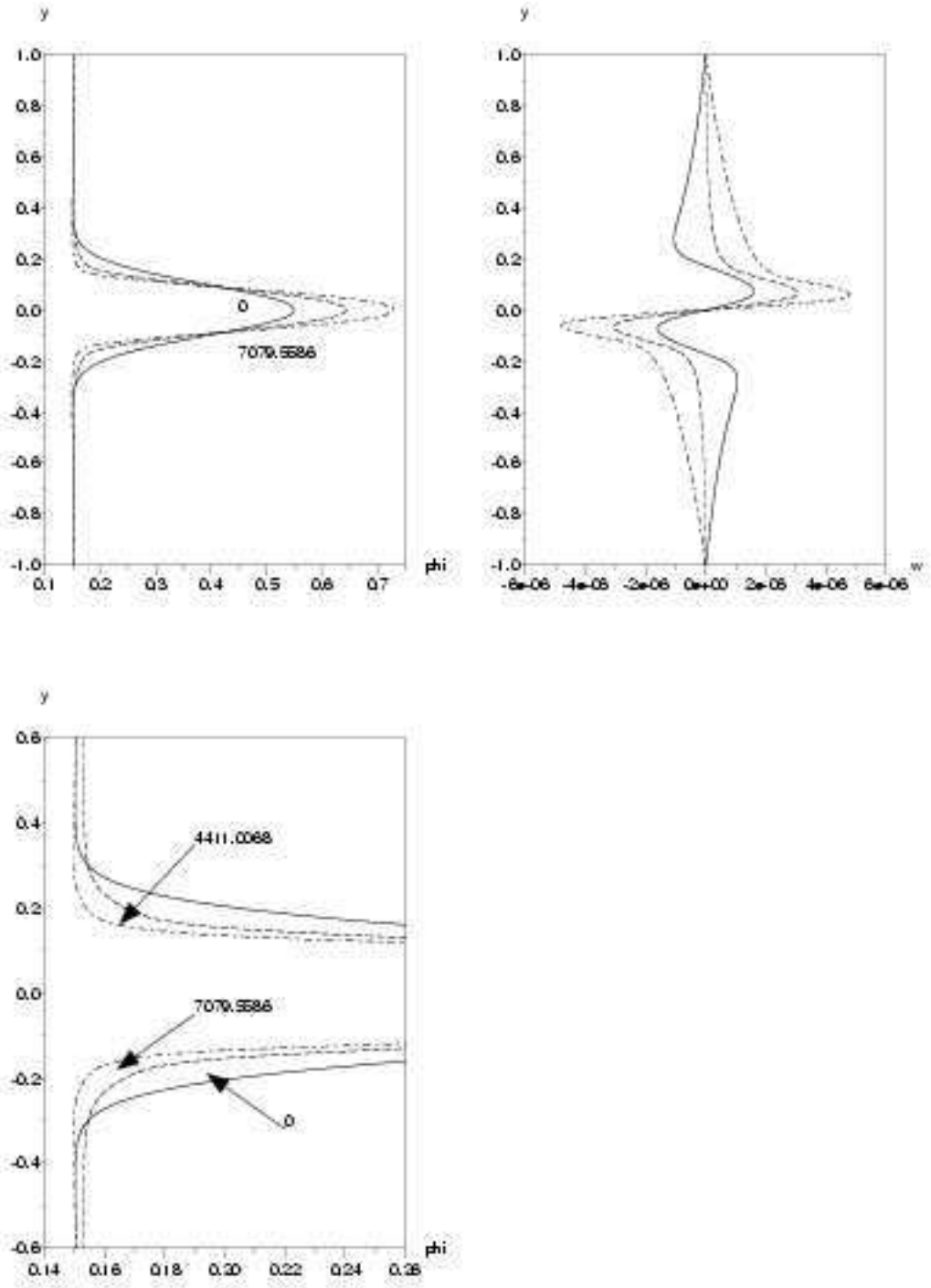

Fig. 5. Surface tension driven self separation of melt distribution. The background melt fraction is below the disaggregation melt fraction and the remains mostly unchanged. (a) Melt distribution at different time steps. (b) Distribution of the matrix velocity. (c) Enlarged view of the plot in (a).For these plots $\xi = 10^{-3}$.

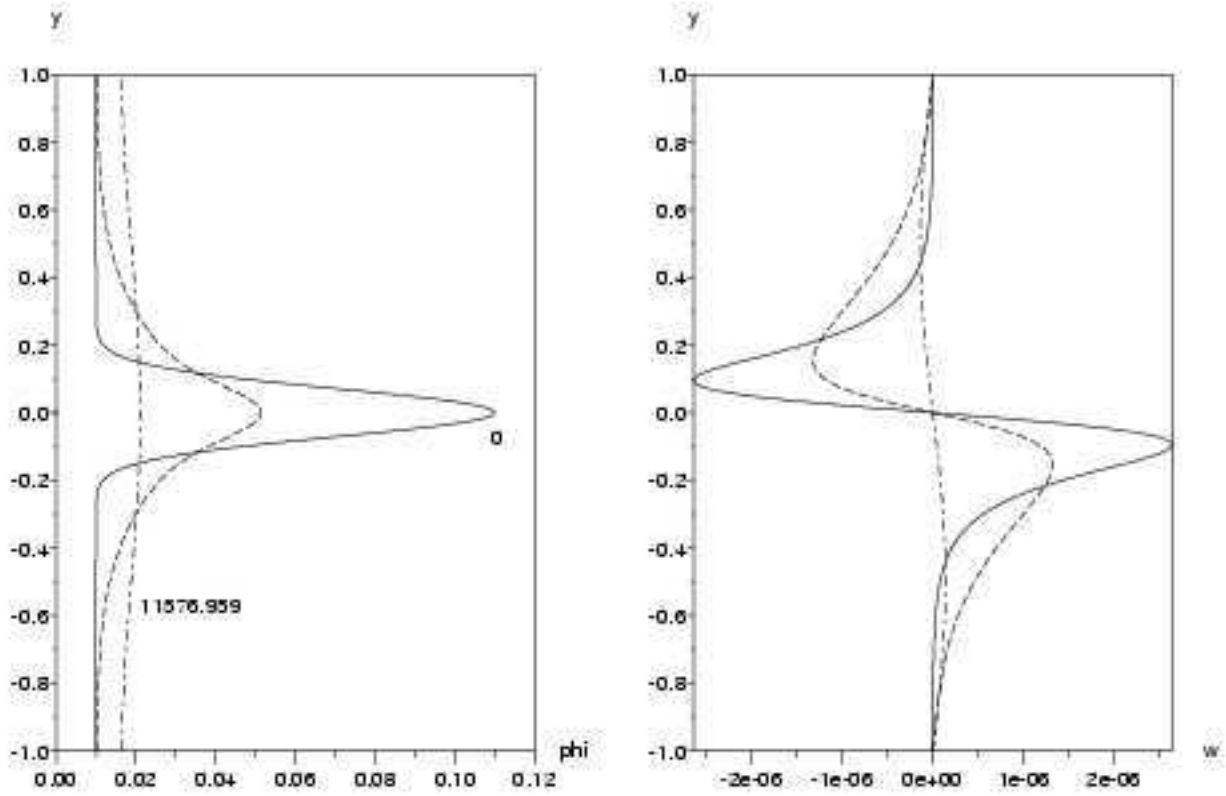

Fig. 6. Homogenization of the melt perturbation by grain boundary wetting.For the plots $\xi = 10^{-3}$.

over a time of 1.2 Ma. The homogenization of the perturbation can be compared to the situation described in the linear analysis. In the linear analysis, we have demonstrated that the growth rate of the perturbations becomes negative for melt fractions below the disaggregation melt fraction. Such diffusive redistribution of basaltic melts driven by grain-grain interfacial tension of silicate minerals has also been experimentally observed (12; 13), for aggregates with small grain size and much smaller length scale. In this formulation, it was possible to incorporate this effect by introducing the function χ given in equation (8). Figure 7 illustrates the normalized differential melt fraction $(\phi_{max} - \phi_0)/(\phi_{max} - \phi_0)_{t=0}$ as a function of time for the three cases discussed above. Curves 'a', 'b', and 'c' correspond to the cases depicted in Figures 4, 5, and 6, respectively. The presence of grain boundaries retard the growth rate of the perturbation in the curve 'b', compared to curve 'a'. Curve 'c' depicts the homogenization of the melt perturbation.

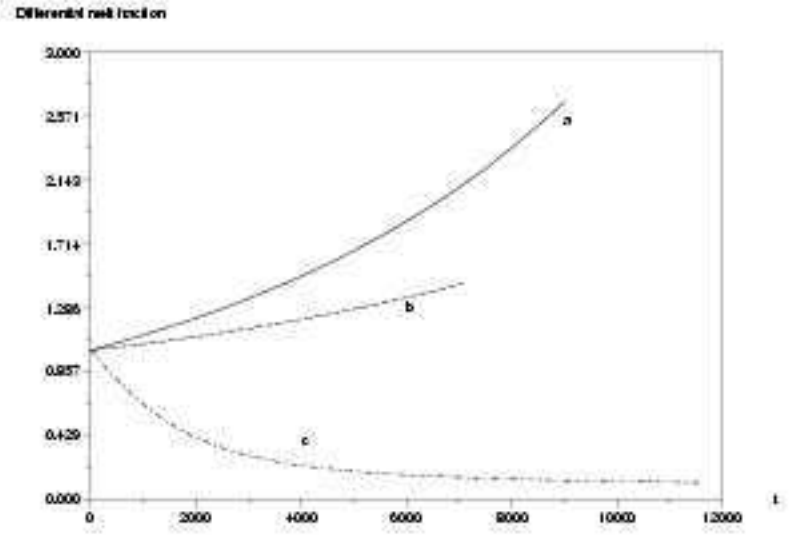

Fig. 7. plot of normalized differential melt fraction $(\phi_{max} - \phi_0)/(\phi_{max} - \phi_0)_{t=0}$ as a function of time. The curves marked 'a', 'b', and 'c' correspond to the cases presented in Figures 4, 5, and 6, respectively.

3.2.2 Gravitation and self separation

In the presence of gravitation, the pattern of melt migration varies strongly depending on the net interfacial tension and the presence of grain boundaries. In this section we consider three cases with $R = 0.1$, but with different surface tension, controlled by ξ, and background melt fractions. In the last two cases, we also demonstrate the difference in the pattern of evolution of the shape of an individual magmon arising due to a change in κ. In this case we solved equations (19) and (20), using a periodic boundary condition.

In the first case we investigate the ascent of buoyant magma in the presence of negligibly small interfacial forces. The plots of evolution of melt distribution in Figure 8 depict the formation of rank ordered wave trains from the initial perturbation, in the presence of a weak interfacial tension force. For these plots $\xi = 1 \times 10^{-6}$. While the background melt fraction ($\phi_0 = 0.01$) is less than the disaggregation melt fraction, the peak of the initial perturbation is more than the disaggregation melt fraction. The initial perturbation breaks up into a series of solitary waves which subsequently travel driven primarily by buoyancy forces. The waves with larger amplitude travel faster than the smaller wave. As seen in the last three plots of Figure 8, the waves nearly retain their shape in collision. However, closer examination may reveal some dispersion during a collision between two wave trains (18). Overall, the formation and dispersion of these wave packets are essentially similar to the porosity waves or magmons, observed in numerical models (19; 20; 21; 22; 18) based on the compaction theory.

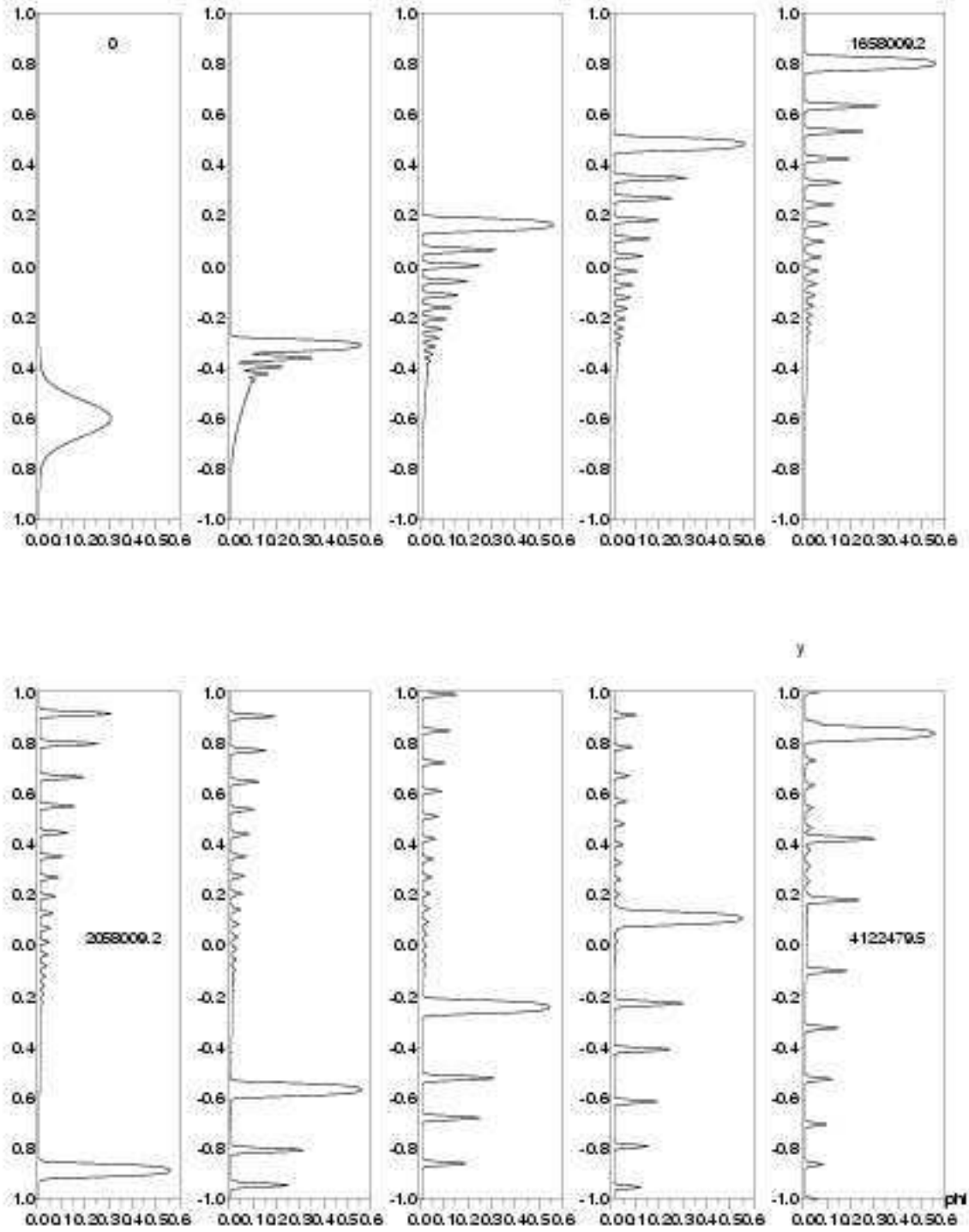

Fig. 8. Ascent of rank ordered traveling porosity waves. Notice the leading waves travel faster the trailing waves with smaller amplitudes. For this plot $\Delta\rho/\rho_m = 0.1, \xi = 0$ and $\delta_m/l = 0.01$. Periodic boundary conditions were used in this simulations.

The surface tension on the grain-grain boundaries influence the evolution of the shape of a magmon. The top and bottom panels in Figure 9 represent two individual magmons with initial background and peak melt fractions of 1 and 30 vol%s. Thus, the background and the peak melt fractions in these magmons are smaller and larger than the disaggregation melt fraction, respectively. For the top panel $\kappa = 1$, whereas for the bottom panel $\kappa = 2$. Both magmons travel ~ 120 km in ~ 260 ka. The enlarged view of the bottom flank of the magmons in the last plots in both panels reveal the influence of the grain-grain interfacial tension. When $\kappa = 1$, the grain-grain interfacial tension is weaker compared to the grain-melt interfacial tension, consequently, the magmon exhibits a self separation like behavior, and melt is drained from the flank into the magmon. On the contrary, the amplitude of the magmon decays during its ascent when $\kappa = 2$. In this case, the magmon is followed by a wake retaining some of the melt. A similar case is illustrated in Figure 10. In this case, the peak and background melt fractions are 15 and 0.5 vol%, both less than the disaggregation melt fraction. The magmon in the bottom panel, corresponding to $\kappa = 2$, decays during its ascent of ~ 70 km in 300 ka. However, the magmon in the top panel, corresponding to $\kappa = 1$, increases slightly in amplitude during ascent. The plots of the peak melt fractions of all these cases are depicted in Figure 11. In both plots, broken and solid lines correspond to $\kappa = 2$ and 1, respectively.

4 Discussions

Interfacial tension due to the grain boundaries modify the melt segregation pattern in solid-liquid aggregates in two different ways. First, in an aggregate composed entirely of the matrix phase, introduction of a localized melt pocket will cause wetting of the grain boundaries of the matrix phase, driven by the interfacial tension of the solid-solid boundaries. This homogenization of the melt distribution will continue until the grain boundaries are completely wetted or until the melt distribution becomes completely homogeneous. The plot in Figure 6 illustrates the later case. Second, in order to dewet the grain boundaries work needs to be done against the the solid-solid interfacial tension. As a consequence, complete melt extraction from a partially wetted aggregate will be substantially hindered. This situation is portrayed in Figure 5, where the background melt fraction remains nearly unaltered while a local perturbation of high melt fraction grows at its own expense.

One important consequence of grain boundary wetting is stable propagation of magmons. Previous works involving two-phase flow indicated that strong surface tension leads to self separation of melt, eventually leading to the formation of stationary sills (10; 11). However, the plot in Figure 5, indicate that the capillary action of the grain boundaries retards melt draining into

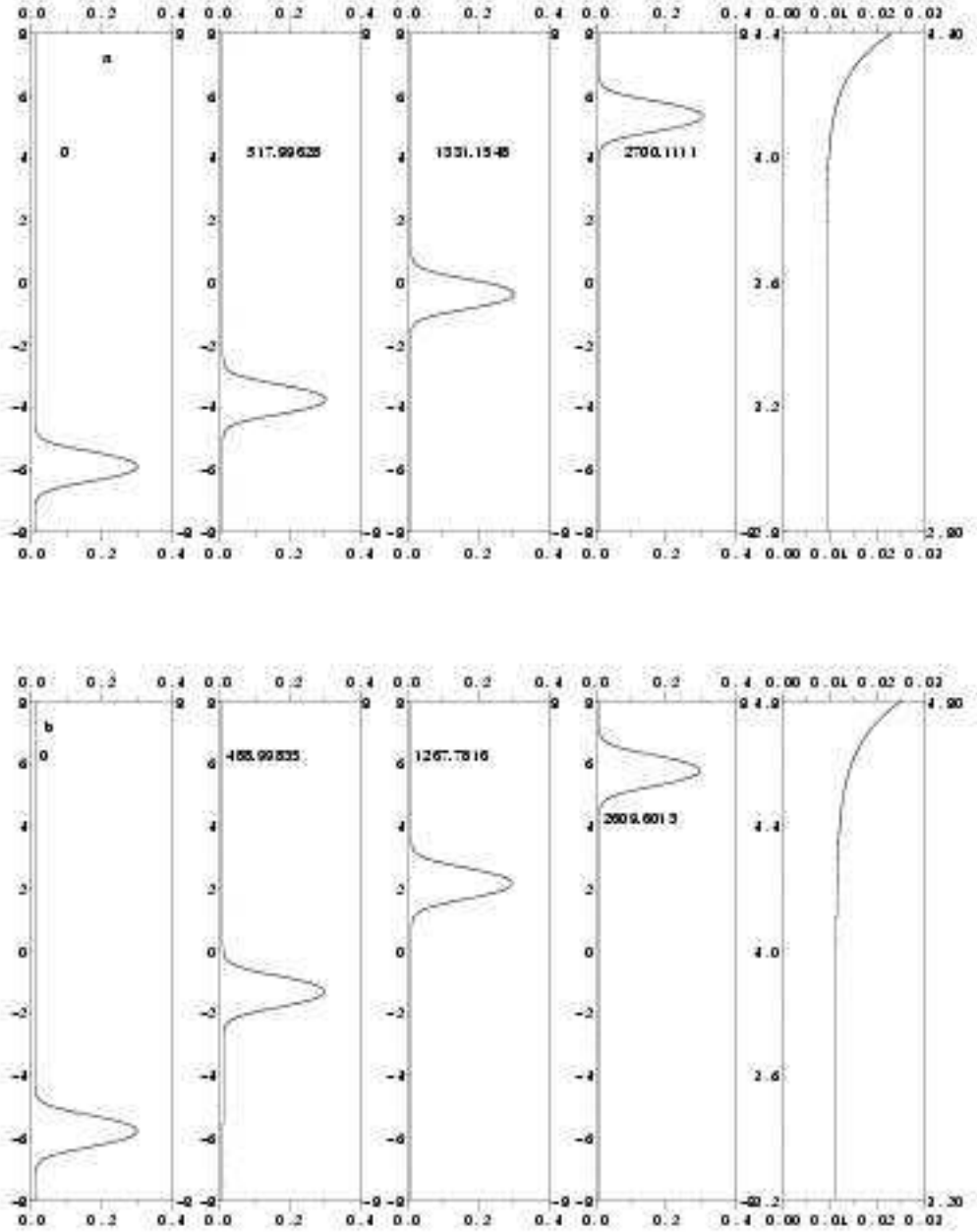

Fig. 9. Ascent of two solitary magma packets. For both plots $\xi = 0.001, R = 0.1$. The last panel in each series is an enlarged view of the bottom flank of the magmons. (a) $\kappa = 1$ and (b)$\kappa = 2$.

stationary sills. However, in the limit of weak interfacial tension on the grain boundaries, the grain-melt interfacial tension prevails and a self separation like behavior is observed.

In regions of melting, gravity drives low density melts away from the source

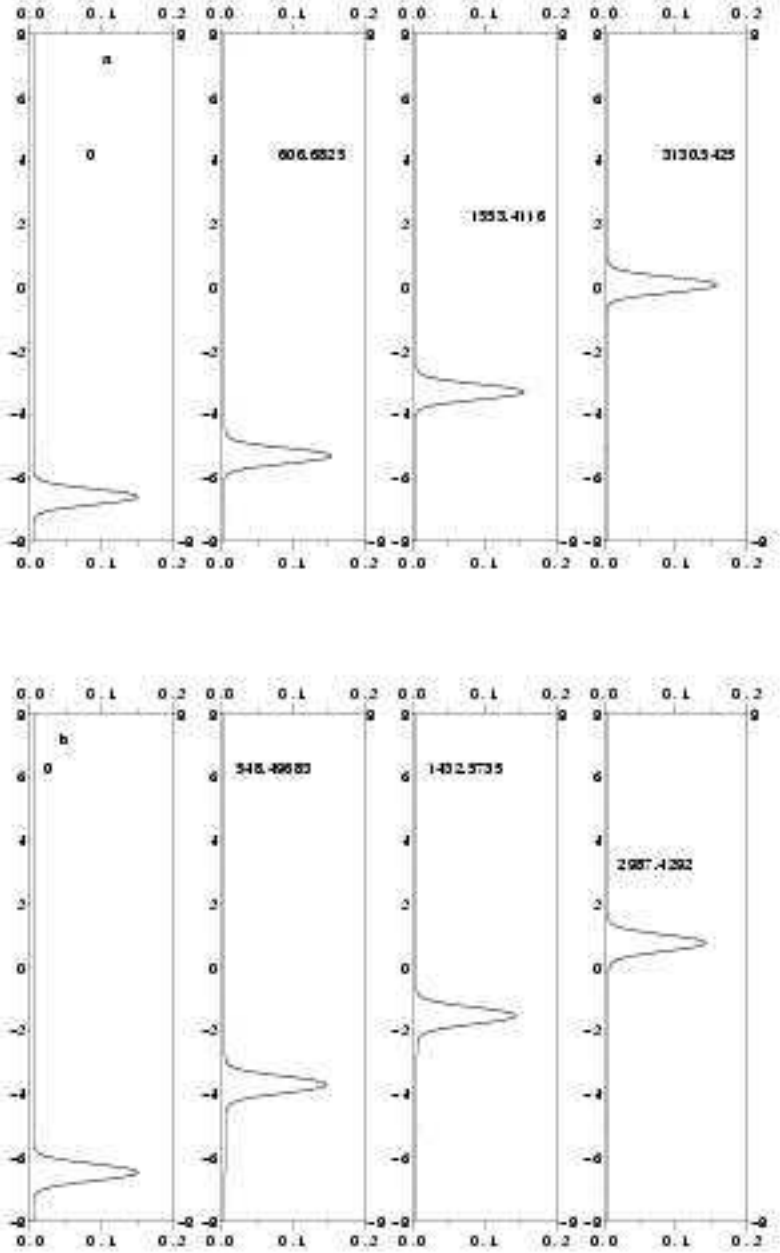

Fig. 10. Ascent of two solitary magmons. (a) $\kappa = 1$ and (b)$\kappa = 2$.

region. However, as demonstrated in the series of plots in the bottom panel of Figure 9, at low background melt fractions, retention of melt by grain boundaries can substantially influence the efficiency of gravity driven melt extraction (5). Small density contrast between the matrix and the melt, or a larger value of ξ, as discussed below, can further impede gravity driven melt extraction from the source region. In an extreme case, a small amount of melt can be trapped in the source region, forming a melt-rich layer.

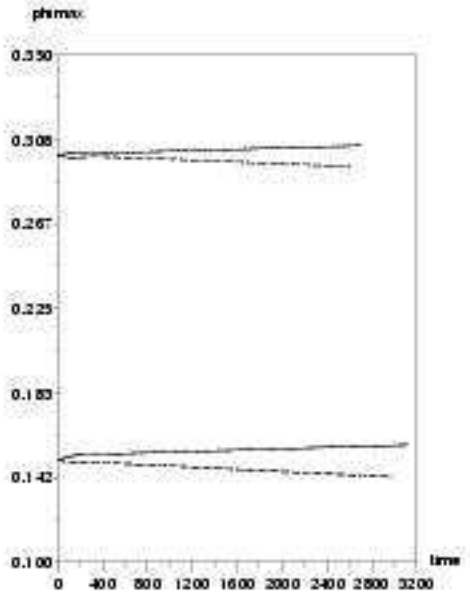

Fig. 11. Plots of peak melt fraction and position of the peak as a function of time during the descent of magma packets illustrated in Figure 9. Broken lines indicate the limit of zero dihedral angle, while solid lines indicate a dihedral angle of 60°.

Another important consequence of partial melt retention by grain boundaries in the matrix is varying degree of metasomatic reactions between the pulse of magmon and the wake. Moreover, the time of metasomatism between a magmon and the mantle rock will also vary depending on the amplitude of the magmon. The magmons illustrated in Figures 9and 9 ascend through 1 m of matrix in 2.2 yr and 4.2 yr. Thus, the chemical signatures in the different magmons and their wakes will also likely be different.

In nature, the influence of interfacial tension compared to buoyancy is determined by the value of the parameter ξ introduced in Section 2.3. On one hand, the series of plots in Figure 8 imply that for a value of $\xi = 10^{-6}$, interfacial tension is negligible compared to buoyancy in geologic times. On the other hand, the plots in figure 9 indicate that for $\xi = 10^{-3}$, interfacial tension drastically influences the rise of buoyant magmons. One geologically relevant parameter controlling the value of ξ, and consequently the influence of interfacial tension is grain size of the matrix (23). The interfacial forces will be most effective in aggregates containing a small average grain size and/or small matrix compaction length. This situation is likely to occur in regions of widespread recrystallization, either following a phase change, such as in the transitions zones, or due to intense deformation such as in shear zones.

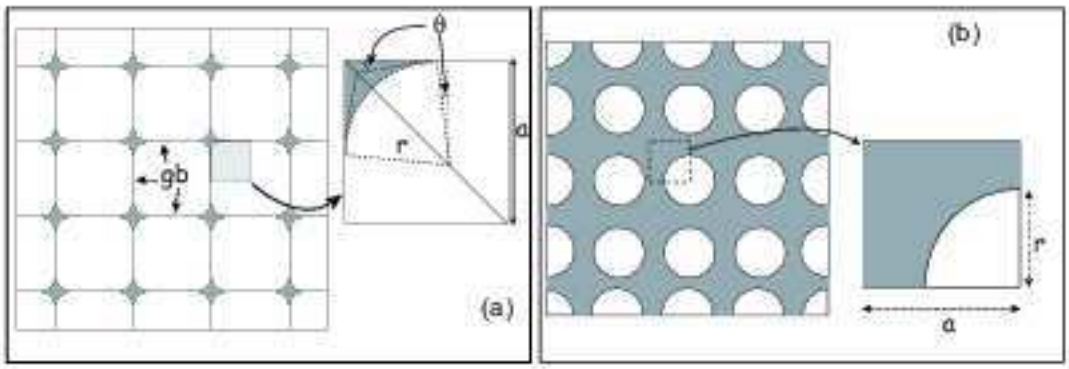

Fig. A.1. Schematic diagram illustrating the face of the control volume for (a) melt fraction less than disaggregation melt fraction, and (b) melt fraction more than disaggregation melt fraction. The angle θ is half of the dihedral angle subtended by two solid-liquid interfaces at the junction with a solid-solid interface.

A The model

In this section we present a simple micro-mechanical model relating the total interfacial tension to the melt fraction. In this model we assume no variation in the third dimension.

For melt fractions below a critical level, given by ϕ_c, both solid-solid and solid-liquid interfaces contribute to the total interfacial tension. The schematic diagram in Figure A.1(a) illustrates the melt distribution on the surface of a control volume, and the shaded region depicts the unit cell for melt fraction less than the disaggregation melt fraction. The total interfacial tension per unit volume χ can be expressed as

$$\chi = \sigma_{ss}a_{ss} + \sigma_{sl}a_{sl}, \tag{A.1}$$

where σ_i and a_i are the interfacial force and interfacial area per unit volume of the interface i, respectively. The quantity a_1 has the dimension of reciprocal of length, see also (9) for the definition of a. The angle θ, subtended by the tangent to the solid-liquid interface to the grain boundary is a material property, related to the ratio of the solid-solid and solid-liquid interfacial tensions, given by

$$\theta = \arccos\frac{\kappa}{2}, \tag{A.2}$$

where $\kappa = \sigma_{ss}/\sigma_{sl}$. The melt can reside in the tubules along grain edges for $0 \leq \kappa \leq 2$. For $\kappa > 2$, grain boundaries are energetically unstable and are readily wetted by the melt. Equation (A.2) is a modified form of Young's equation, see (24; 25) for a more detailed derivation. The volume fraction of melt can be expressed as a function of the radius of curvature r of the

solid-liquid interface and the dihedral angle θ as

$$\phi = \left(\frac{r}{a}\right)^2 \left(\cos^2\theta - \sin\theta\cos\theta - \frac{\pi}{4} + \theta\right), \tag{A.3}$$

where a is the size of the unit cell, which is one-fourth of the average grain size. It is also possible to express α_i as a function of r, θ and a, and using the relation given in equation (A.3), as a function of ϕ. The expressions for α_i become,

$$\frac{\alpha_{sl}}{\alpha_0} = \left|\frac{\pi}{2} - 2\theta\right| \left(\frac{r}{a}\right) = \frac{\left|\frac{\pi}{2} - 2\theta\right|}{\sqrt{\cos^2\theta - \sin\theta\cos\theta - \frac{\pi}{4} + \theta}} \sqrt{\phi}, \tag{A.4}$$

and

$$\frac{\alpha_{ss}}{\alpha_0} = 1 - \left(\frac{r}{a}\right) |\cos\theta - \sin\theta| = 1 - \frac{|\cos\theta - \sin\theta|}{\sqrt{\cos^2\theta - \sin\theta\cos\theta - \frac{\pi}{4} + \theta}} \sqrt{\phi}, \tag{A.5}$$

where $\alpha_0 = 1/a$ is the volume fraction of grain boundary or solid-solid surface area at $\phi = 0$. The expressions in equations (A.4) and (A.5), indicate that the solid-liquid interfacial area increases with an increase in the melt fraction while the solid-solid interfacial area decreases with increasing melt fraction. Finally, we combine equations (A.1), (A.4), and (A.5) to obtain

$$\chi = \alpha_0 \left[\sigma_{sl}\chi_1\sqrt{\phi} + \sigma_{ss}\left(1 - \chi_2\sqrt{\phi}\right)\right], \text{for} \phi < \phi_c \tag{A.6}$$

where

$$\chi_1 = \frac{\left|\frac{\pi}{2} - 2\theta\right|}{\sqrt{\cos^2\theta - \sin\theta\cos\theta - \frac{\pi}{4} + \theta}}, \tag{A.7}$$

and

$$\chi_2 = 1 - \frac{|\cos\theta - \sin\theta|}{\sqrt{\cos^2\theta - \sin\theta\cos\theta - \frac{\pi}{4} + \theta}}. \tag{A.8}$$

At the disaggregation melt fraction, the grain boundaries are completely wetted, and accordingly the radius of curvature of the solid-liquid interface is not controlled by the dihedral angle anymore. In liquid phase sintering of two-phase aggregates, such a jump in the radius of curvature caused by coalescence/decohesion of two solid grains are observed frequently (26, section 5E). The evolution of the solid-liquid interfacial area can now be described by the area of cylindrical grains shrinking uniformly with increasing melt fraction. The diagram in Figure A.1(b) indicates that under this situation,

$$\phi = 1 - \frac{\pi}{4}\left(\frac{r}{a}\right)^2, \tag{A.9}$$

while

$$a_{sl} = a_0 \sqrt{\frac{\pi}{4}(1-\phi)}. \tag{A.10}$$

Plugging equation (A.10) back into equation (A.1), one obtains

$$\chi = \sigma_{sl} a_0 \sqrt{\frac{\pi}{4}(1-\phi)} \quad \text{for} \quad \phi > \phi_c. \tag{A.11}$$

The schematic diagram in Figure A.1(a) illustrates a case where the curvature of the fluid interface is concave toward the solid grain, indicating $\theta < \pi/4$. However, the relations given in equations (A.4) and (A.5) are also valid for $\theta > \pi/4$, when the solid-liquid interface is convex towards the solid grain. In the case of pores with straight walls, one can follow a similar formalism

B Energy conservation

Following (9: 16), the total energy balance for a two phase aggregate is given by:

$$\overline{\rho c}\frac{\bar{\bar{D}}T}{Dt} + \frac{\bar{D}(\xi_i a)}{Dt} = Q - \nabla \cdot \mathbf{q} + \Psi - \Delta P \frac{\bar{D}\phi}{Dt} + (\sigma a - \xi_i a)\nabla \cdot \bar{\mathbf{v}}, \tag{B.1}$$

where the material derivatives $\bar{\bar{D}}/Dt$ and $\bar{D}/Dt$ are averaged over the matrix and the fluid material derivatives as defined in (9: 16). The quantity ξ_i is the energy per unit of the interfacial area of the control volume. We define this quantity as

$$\xi_i = \sigma(\phi, T) - T\frac{\partial \sigma(\phi, T)}{\partial T}, \tag{B.2}$$

where σ is the average surface tension per unit area of the control volume. We also define $a(\phi)$ as the interfacial area in one unit of the control volume. After some algebra, equations (B.1) and (B.2) can be reduced to,

$$\begin{aligned} &\overline{\rho c}\frac{\bar{\bar{D}}T}{Dt} - T\frac{\bar{D}}{Dt}\left(a\frac{\partial \sigma}{\partial T}\right) - aT\frac{\partial \sigma}{\partial T}\nabla \cdot \bar{\mathbf{v}} \\ &= Q - \nabla \cdot \mathbf{q} + \Psi - \left(\Delta P + \frac{\partial(\sigma a)}{\partial \phi}\right)\frac{\bar{D}\phi}{Dt}. \end{aligned} \tag{B.3}$$

The terms on the left hand side of equation (B.3) are associated with entropy production.

The mechanical work terms on the right hand side of equation (B.3) can be further divided into reversible and irreversible work. The reversible components of mechanical work comprises of work done to deform the interface, to

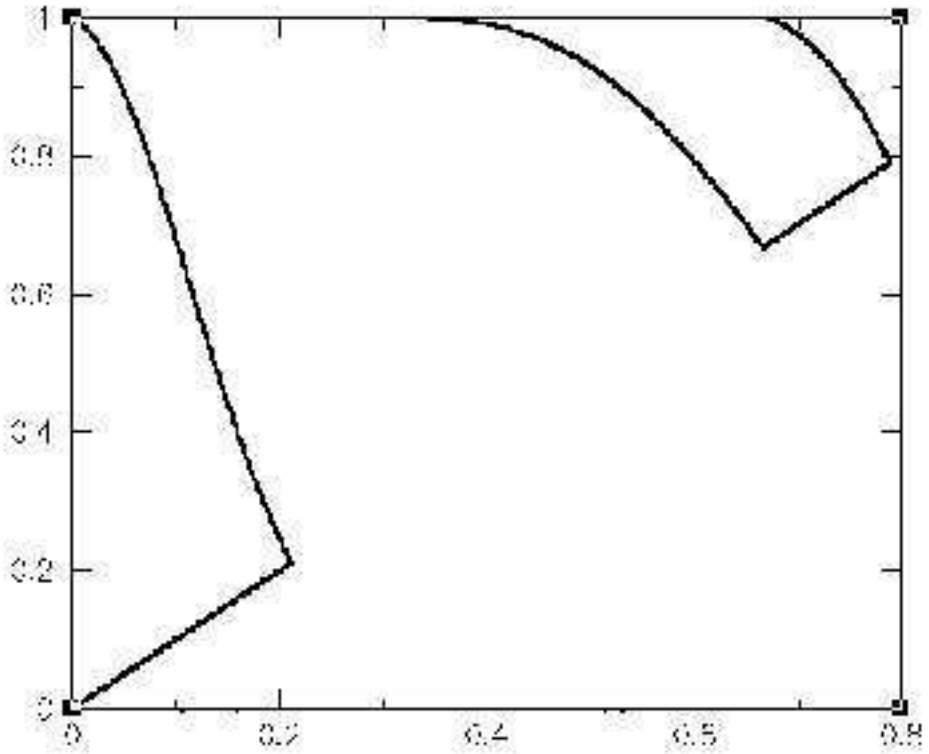

Fig. C.1. A map of the real solutions to equation (C.4) in the $\Phi_0 - \Phi_m$ space. The gray region indicates permissible real solutions, while the black region indicates complex solutions to equation (C.4). Solutions do not have any physical meaning in the white region since in this region, the background melt fraction is larger than the peak melt fraction.

isotropically compact or dilate the matrix, and the work done by the interfacial pressure. Thus, the equation for reversible work becomes (16, equation 20) :

$$\frac{\partial(\sigma\alpha)}{\partial\phi}\frac{\tilde{D}\phi}{Dt} = -\Delta P\frac{\tilde{D}\phi}{Dt} - \frac{K_0\mu_m}{\phi(1-\phi)}\left(\frac{\tilde{D}\phi}{Dt}\right)^2. \tag{B.4}$$

In this work we define the quantity $\chi = \sigma\alpha$, as discussed in Appendix A. Thus, equation (B.4) can be rewritten as:

$$\frac{\partial\chi}{\partial\phi} = -\Delta P - \frac{K_0\mu_m}{\phi(1-\phi)}\frac{D_m\phi}{Dt}. \tag{B.5}$$

C Analytical solution

We seek a solution to equations (19) and (20) of the form

$$\phi = \Phi(f), \tag{C.1}$$

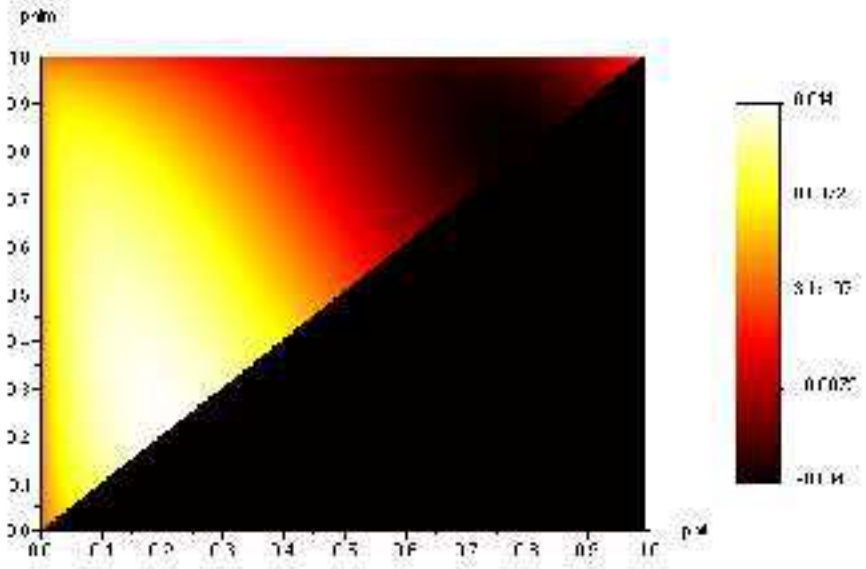

Fig. C.2. A map of the solitary wave velocity c, in the $\Phi_0 - \Phi_m$ space. The velocity of the solitary waves are given by equation (C.6).

where $f = y - ct$ is the characteristic variable with c being the velocity of the solitary wave.

Integrating equation (19) yields,

$$w = -\frac{c\,\Phi + K_1}{1-\Phi}, \tag{C.2}$$

where K_1 is a constant of integration. Substituting the matrix velocity from equation (C.2) into equation (20) we obtain, for $\xi = 0$,

$$0 = -\frac{4}{3}(c+K_1)\left[\frac{(1+\Phi)\Phi'}{\Phi(1-\Phi)}\right]' - R(1-\Phi) + \frac{4}{3}\frac{c\Phi + K_1}{(1-\Phi)\Phi^2}. \tag{C.3}$$

Next, we multiply both sides of equation (C.3) by $[(1+\Phi)\Phi']/[\Phi(1-\Phi)]$ and integrate to obtain,

$$0 = \left(\frac{c+K_1}{2}\right)\left(\frac{1+\Phi}{\Phi(1-\Phi)}\Phi'\right)^2 + \frac{3R}{4}(\Phi + \ln\Phi) \tag{C.4}$$
$$+ \left[\frac{c+3K_1}{\Phi} + \frac{K_1}{2\Phi^2} - \frac{2(c+K_1)}{1-\Phi} - (3c+5K_1)\ln\left(\frac{\Phi}{1-\Phi}\right)\right] + K_2.$$

In order to determine the constants of integration K_i, we use a criterion suggested by (15) for a 'witch hat' solitary wave function. The solitary wave function Φ assumes a constant value of Φ_0 in the background and the maximum value Φ_m at the peak, implying $\Phi' = \Phi'' = 0$ when $\Phi = \Phi_0$ and $\Phi' = 0$ when

$\Phi = \Phi_m$. Thus we obtain the values of the constant K_1 from equation (C.3) for $\Phi = \Phi_0$ and the value of constant K_2 from equation (C.4), for $\Phi = \Phi_m$. The constants K_i are given by,

$$K_1 = \frac{3R}{4}(1-\Phi_0)^2\Phi_0^2 - c\Phi_0, \quad \text{(C.5)}$$

$$K_2 = -\left[\frac{c+3K_1}{\Phi_m} + \frac{K_1}{2\Phi_m^2} - \frac{2(c+K_1)}{1-\Phi_m} - (3c+5K_1)\ln\left(\frac{\Phi_m}{1-\Phi_m}\right)\right] - \frac{3R}{4}\left(\Phi_m + \ln(\Phi_m)\right).$$

The velocity c of an individual solitary wave is controlled by the background melt fraction Φ_0 and the amplitude Φ_m of the solitary wave. We can obtain the velocity of the solitary wave c as a function of the peak and background melt fractions, by substituting $\Phi = \Phi_m$ in equation (C.4), and noticing that $\Phi' = 0$ at $\Phi = \Phi_m$. Equation (C.4) yields,

$$c = \frac{\Phi_1 + \frac{3R}{4}\Phi_0^2(1-\Phi_0)^2\Phi_3}{\Phi_0\Phi_3 - \Phi_2} \quad \text{(C.6)}$$

where the functions Φ_1, Φ_2, and Φ_3 depend on Φ_0 and Φ_m, and are given by

$$\begin{aligned}
\Phi_1 &= \frac{3R}{4}\left(\Phi_m - \Phi_0 + \ln\left(\frac{\Phi_m}{\Phi_0}\right)\right), \\
\Phi_2 &= \left(\frac{1}{\Phi_m} - \frac{1}{\Phi_0}\right) - \left[2\left(\frac{1}{1-\Phi_m} - \frac{1}{1-\Phi_0}\right) + 3\ln\left(\frac{(1-\Phi_0)\,\Phi_m}{(1-\Phi_m)\,\Phi_0}\right)\right], \quad \text{(C.7)} \\
\Phi_3 &= \frac{1}{2}\left(\frac{1}{\Phi_m^2} - \frac{1}{\Phi_0^2}\right) + 3\left(\frac{1}{\Phi_m} - \frac{1}{\Phi_0}\right) \\
&\quad - \left[2\left(\frac{1}{1-\Phi_m} - \frac{1}{1-\Phi_0}\right) + 5\ln\left(\frac{(1-\Phi_0)\,\Phi_m}{(1-\Phi_m)\,\Phi_0}\right)\right].
\end{aligned}$$

Stable, real solitary wave solutions are permitted only over a range of possible combinations of the background and peak melt fractions. A real solution to equation (C.4) does not exist for $(\Phi')^2 < 0$. The map in Figure C.1 illustrates the range of real solutions to the solitary wave equation in the $\Phi_0 - \Phi_m$ space. The areas shaded in gray indicate regions where a real solution exist, whereas regions shaded black indicate that the solution is complex. Since the wave cannot exist if the peak melt fraction is less than the background melt fraction, no physically meaningful solution exist in the white region.

The velocities of the solitary waves in the two possible branches of solution domain are opposite in sign. Figure C.2 depicts a map of the solitary wave velocity c in the $\Phi_0 - \Phi_m$ space as indicated in equation (C.6). In the map,

the peak in the positive velocity correspond to the first branch in the solution domain, whereas the peak in the negative velocity correspond to the the second branch in the solution domain.

Finally, we integrated equation (C.4) numerically employing a fourth order Runge-Kutta method. Since at $t = 0, \Phi(f) = \Phi(y)$, the numerically integrated function Φ was used as the initial condition for some of the solitary wave solutions presented in section 3.2.2.

References

[1] G. Hirth, D. L. Kohlstedt, Experimental constraints on the dynamics of the partially molten upper mantle: deformation in the diffusion creep regime, Journal of Geophysical Research, B, Solid Earth and Planets 100 (2) (1995) 1981–2001.

[2] R. Cooper, D. Kohlstedt, K. Chyung, Solution-precipitation enhanced creep in solid-liquid aggregates which display a non-zero dihedral angle, Acta Metallurgica 37 (7) (1989) 1759–1771.

[3] S. Hier-Majumder, I. Anderson, D. Kohlstedt, Influence of protons on Fe-Mg interdiffusion in olivine, Journal of Geophysical Research, B, Solid earth and Planets 110 (2005) xx.

[4] N. von Bargen, H. Waff, Permeabilities, interfacial areas and curvatures of partially molten systems: results of numerical computations of equilibrium microstructures, J. Geophys. Res. 91 (1986) 9261–9276.

[5] R. Dasgupta, M. Hirschmann, A. Withers, Deep global cycling of carbon constrained by the solidus of anhydrous, carbonated eclogite under upper mantle conditions, Earth and Planetary Science Letters 227 (2004) 73–85.

[6] D. Drew, L. Segel, Averaged equations for two-phase flows, Stud. Appl. Math. 50 (1971) 205–257.

[7] D. Drew, Averaged field equations for two-phase flow, Annu. Rev. Fluid Mech. 15 (1983) 261–291.

[8] D. Drew, S. Passman, Theory of Multicomponent Fluids, Vol. 135 of Appl. Math. Sci., Springer-Verlag, New York, 1999.

[9] D. Bercovici, Y. Ricard, G. Schubert, A two-phase model for compaction and damage: 1, general theory, Journal of Geophysical Research, B, Solid Earth and Planets 106 (5) (2001) 8887–8906.

[10] Y. Ricard, D. Bercovici, G. Schubert, A two-phase model for compaction and damage: 2, applications to compaction, deformation, and the role of interfacial surface tension, Journal of Geophysical Research, B, Solid Earth and Planets 106 (5).

[11] D. Bercovici, Y. Ricard, G. Schubert, A two-phase model for compaction and damage: 3, applications to shear localization and plate boundary

formation, Journal of Geophysical Research, B, Solid Earth and Planets 106 (5) (2001) 8925–8939.

[12] G. Riley Jr, D. Kohlstedt, F. Richter, Melt migration in a silicate liquid-olivine system: An experimental test of compaction theory, Geophys. Res. Lett. 17 (1990) 2101–2104.

[13] G. Riley Jr, D. Kohlstedt, Kinetics of melt migration in upper mantle-type rocks, Earth Planet. Sci. Lett. 105 (1991) 500–521.

[14] D. Stevenson, On the role of surface tension in the migration of melts and fluids, Geophys. Res. Lett. 13 (1986) 1149–1152.

[15] M. Rabinowicz, Y. Ricard, M. Grégoire, Compaction in a mantle with a very small melt concentration: Implications for the generation of carbonatitic and carbonate-bearing high alkaline mafic melt impregnations, Earth and Planetary Science Letters 203 (2002) 205–220.

[16] D. Bercovici, Y. Ricard, Energetics of two-phase model of lithospheric damage, shear localization and plate-boundary formation., Geophysical Journal International 152 (3) (2003) 581–596.

[17] D. Turcotte, G. Schubert, Geodynamics, John Willey & Sons, 1999.

[18] V. Barcilon, F. Richter, Nonlinear waves in compacting media, J. Fluid Mech. 164 (1986) 429–448.

[19] D. Scott, D. Stevenson, Magma solitions, Geophys. Res. Lett. 11 (1984) 1161–1164.

[20] D. Scott, D. Stevenson, Magma ascent by porous flow, J. Geophys. Res. 91 (1986) 9283–9296.

[21] D. Scott, The competition between percolation and circulation in a deformable porous medium, J. Geophys. Res. 93 (1988) 6451–6462.

[22] M. Spiegelman, Flow in deformable porous media, part 2, numerical analysis–the relationship between shock waves and solitary waves, J. Fluid Mech. 247 (1993) 39–63.

[23] D. Wark, E. Watson, Effect of grain size on the distribution and transport of deep-seated fluids and melts, Geophysical Research Letters 27 (14) (2000) 2029–2032.

[24] F. C. Goodrich, The thermodynamics of fluid interfaces, in: E. Matijević (Ed.), Surface and Colloid Science, Willey-Interscience, New York, 1969, pp. 33–37.

[25] R. E. Johnson Jr., Conflicts between gibbsian thermodynamics and recent treatments of interfacial energies in solid-liquid-vapor systems, Journal of Physical Chemistry 63 (10) (1959) 1655–1658.

[26] R. German, Liquid Phase Sintering, Plenum Press, 1985.